

# Detection of near-surface heterogeneities at archaeological sites using seismic diffractions

Jianhuan Liu<sup>1\*</sup>, Quentin Bourgeois<sup>2</sup>, Ranajit Ghose<sup>1</sup> and Deyan Draganov<sup>1</sup> propose an approach for imaging subsurface objects using masked diffractions.

## Introduction

The detection of shallow buried ancient structures or objects of cultural heritage is a primary challenge for seismic surveys at archaeological sites. The knowledge of the distribution of shallow objects can assist archaeologists' study of the past without making excavations. Excavations lead to surface exposure of the buried objects and potential damages and preservation issues. The seismic response arising from localized archaeological targets is encoded in diffractions, which can be used to locate the objects. However, the energy of a diffracted wave is usually weak and masked behind the strong presence of other coherent signals or coherent noise in the data (e.g., surface waves, specular reflections). This makes it difficult to detect and interpret reliably.

In the past decades, researchers have attempted to detect various near-surface features using diffracted waves. Landa and Keydar (1998) developed a method for identifying local targets in the shallow subsurface using diffracted waves. They constructed a so-called diffraction-point-section (D-section) by concentrating diffracted waves from diffractor points. The anomalies in this D-section can be interpreted as potential scattering objects. Shtivelman and Keydar (2005) proposed a multipath summation approach to image near-surface objects by stacking diffracted energy along all possible diffraction curves defined by all velocity values within a specific range. Subsequently, Shtivelman et al. (2009) improved the resolution of this multipath summation approach by introducing image-dependent weights.

The above-mentioned methods have been tested earlier on field data dominated by surface waves; no identification of diffracted waves could be found. To improve the reliability of diffraction imaging, in this paper we first apply a method that consists of seismic interferometry (SI) and adaptive subtraction for the suppression of high-amplitude surface-wave noise (Konstantaki et al., 2015; Liu et al., 2018). We then present an approach based on an extension of the spatial summation of weak diffractions as proposed by Shtivelman and Keydar (2005). We utilize instantaneous-phase coherency (Schimmel and Paulssen, 1997) to enhance the optimal summation of weak but coherent diffractions.

In the following, we first describe the practical steps for the implementation of each of the above methods. We then

demonstrate the feasibility of our approach in locating scatterers on numerically modelled data with a low signal-to-noise ratio (S/N). Finally, we test our method on field seismic data acquired at an archaeological site.

## Methodology

### Surface-waves removal

SI refers to the retrieval of new seismic responses between two receivers by, most commonly, cross-correlating the wavefields observed at these receivers from surrounding sources and stacking the cross-correlations for all the sources (Draganov et al., 2006; Wapenaar and Fokkema, 2006). For a near-surface seismic survey, the active sources are located along the surface of the earth. Such a source configuration will make the results retrieved by SI dominated by surface waves. Because of this, we make use of SI to retrieve the dominant surface waves contained in the field data. A non-stationary matching filter (Fomel, 2008) is then estimated to adaptively subtract the retrieved surface waves from the raw data, while preserving the weak diffraction events. For the implementation details of this surface-waves suppression scheme, we refer the readers to Liu et al. (2018).

### Diffraction imaging

Assume a diffractor located at  $(X_D, Z_D)$  in a homogeneous medium. For an arbitrary source located at  $(X_S, 0)$ , a part of the wavefield generated by this source will first travel downward and hit the diffractor. It will then be diffracted back to the surface and recorded by a receiver positioned at  $(X_R, 0)$ . The traveltime curve of this diffracted event can be expressed as

$$T_{SR} = \sqrt{\left(\frac{X_D - X_S}{V}\right)^2 + \left(\frac{T_D}{2}\right)^2} + \sqrt{\left(\frac{X_R - X_D}{V}\right)^2 + \left(\frac{T_D}{2}\right)^2}. \quad (1)$$

In equation (1), the first term on the right-hand side is the source-diffractor traveltime, whereas the second term is the diffractor-receiver traveltime.  $V$  is the near-surface velocity,  $T_D$  is the two-way vertical traveltime when source, diffractor, and receiver share the same lateral position.

We assume that every subsurface point is a candidate diffractor which can cause a diffracted event. For every point to be

<sup>1</sup> Delft University of Technology, The Netherlands | <sup>2</sup> University of Leiden, The Netherlands

\* Corresponding author, E-mail: j.liu-4@tudelft.nl

\*\* This paper is part of the August Special Topic on Near Surface Geoscience. Due to a last minute change in production planning this paper was unfortunately left out.

imaged, the seismic data are stacked along a specific diffraction trajectory defined by equation (1); this results in a final stacked time section where diffracted energy is optimally focused.

Next, we describe the practical implementation steps of this diffraction-stacking method. For a specific source gather, we first assume that the diffractor is located directly under the first receiver. This will lead to a specific diffraction traveltime curve according to equation (1), where  $X_D$  is the lateral location of the first receiver. Next, we apply diffraction-moveout correction to this source gather and obtain a new gather. Such a traveltime correction procedure is repeated for all other combinations of source-receiver pairs. This will result in  $ns \times nr$  gathers corrected for diffraction moveout, where  $ns$  and  $nr$  are the number of sources and receivers, respectively. These moveout-corrected source gathers are then sorted into common-receiver gathers and stacked to produce one single trace per receiver position. To further enhance the coherent summation along weak diffractions, the stacked trace is then weighted by amplitude-unbiased coherency factors (Schimmel and Paulssen, 1997). The coherency for each stacked trace is calculated from the traces involved in the stacking of the common-receiver gather used to obtain that trace using

$$C(t) = \frac{1}{N} \left| \sum_{j=1}^N e^{i\phi_j(t)} \right|^v, \quad (2)$$

where  $N$  is the number of traces used,  $\phi_j(t)$  is the instantaneous phase of the  $j$ -th trace obtained by complex trace analysis (Bracewell, 1986). The parameter  $v$  controls the transition between more coherent and less coherent signal summations; here we use  $v=2$  as suggested by Schimmel and Paulssen (1997).

The stacked traces weighted by equation (2) from each common-receiver gather are then assembled into a diffraction section (Landa and Keydar, 1998; Walters et al., 2009), where anomalies indicate the spatial location of diffractors. When the near-surface

velocity  $V$  is not available, we can iterate the above procedures over a specific range of velocity values (Shtivelman and Keydar, 2005; Shtivelman et al., 2009). In this way, the diffraction energy can be coherently focused to produce a final image.

## Examples

### Synthetic data

The model shown in Figure 1a includes seven randomly distributed point diffractors at shallow depths in a homogeneous medium with a background velocity of 150 m/s. The receiver array consists of 120 geophones, starting from 0 m to 29.75 m at 0.25 m intervals. This array remains fixed, while the source advances with a step of 2 m. The first source is located at 4 m before the first geophone, while the last source is placed 7.5 m after the last geophone. With this acquisition geometry, 21 common-shot gathers (Figure 2a) are computed using an acoustic finite-difference algorithm (Thorbecke and Draganov, 2011). Band-pass-filtered Gaussian random noise ( $S/N = 0.008$ ) is then added to the clean synthetic gathers to build a new dataset. Figure 2b illustrates one noisy common-source gather for a source positioned at 16 m. We use this noisy dataset to demonstrate the feasibility of our approach to detect shallow diffractors.

Our new algorithm is designed to focus coherently the diffraction energy back to its original position while suppressing all other incoherent events through directional summation. This procedure will make the true diffractions appear as a high-amplitude anomaly in the resulting section. Figure 1b represents the diffraction imaging section derived from the noisy data through our diffraction-enhancement approach. In Figure 1b, the horizontal axis denotes the lateral location (in m), while the vertical axis is the approximate depth (in m) that we obtain using the true subsurface velocity. The range of velocities used for diffraction summation is from 140 m/s to 160 m/s with a step of 5 m/s. We display the final time section (Figure 1b) using semblance calculated from diffraction sections obtained from each velocity used for stacking. We can clearly identify seven prominent anomalies in Figure 1b, after significant suppression of the highly uncorrelated noise that is present in the original data. The maximum amplitudes of these anomalies can be interpreted as the centers of the diffractors, which correspond well with the true locations of the diffractors embedded in the synthetic model (Figure 1a).

### Field data

In 2017 we acquired seismic data at an archaeological burial mound located in the Veluwe, the Netherlands. Burial mounds are the most widespread prehistoric graves and are clearly visible as low hillocks to this day. In the Veluwe, about 50 such burial mounds are well-preserved and are distributed along an approximately 6 km-long line. Most of these burial mounds can be dated back to about 5000 years ago (Bourgeois, 2012). The mound that we investigated is labelled as Mound B4749, and it is located in the middle of the woods of the Veluwe.

To illuminate near-surface small objects underneath Mound B4749, we deployed an array of 120 horizontal 10 Hz single-component geophones over the top of this mound. We acquired two types of seismic data - using a sledge-hammer (shear-wave) and

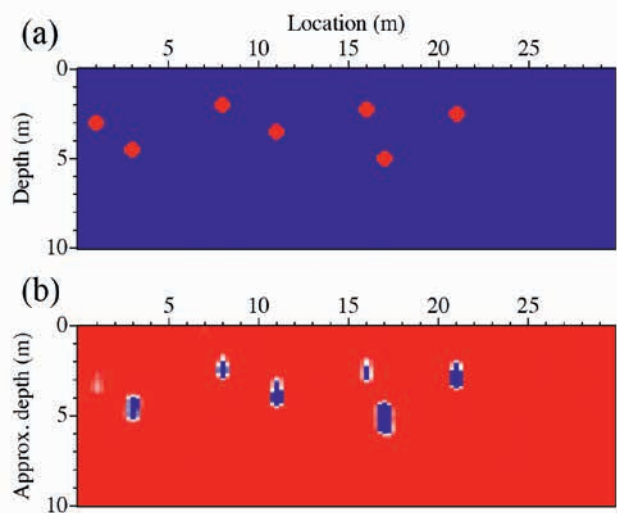


**Figure 1** (a) Model used to generate the synthetic common-source gathers. Seven shallow diffractors with a certain impedance contrast with respect to the background medium are embedded in this model. The background velocity is 150 m/s. (b) Result of diffraction imaging through diffraction summation weighted by instantaneous-phase coherence. Seven high-amplitude anomalies can be identified in Figure 1 (b), whose positions are very close to the true locations of the diffractors in the synthetic model. Note that the shapes of these anomalies do not necessarily correspond to the actual shapes of the objects.

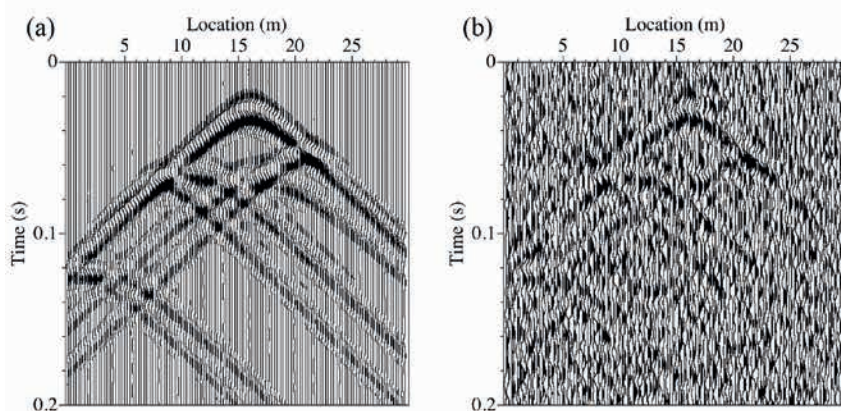


**Figure 2** Typical example of a synthetic common-source gather for a source located at 16 m.  
(a) Common-source gather modelled without direct waves. (b) The same gather after adding highly uncorrelated random noise ( $S/N = 0.008$ ).

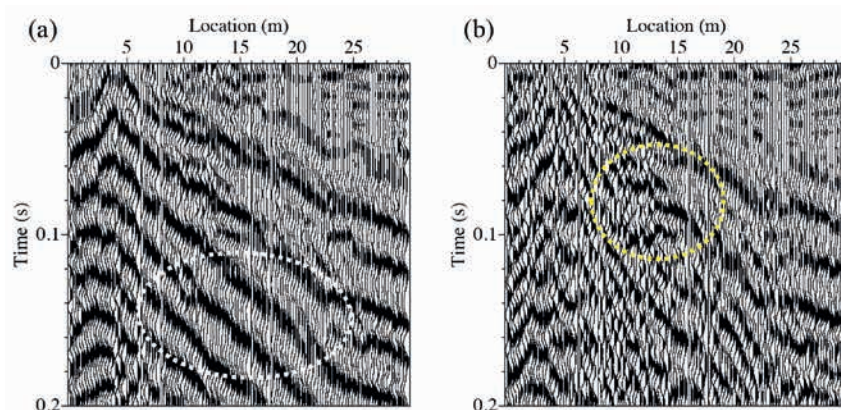


**Figure 3** (a) A shot gather contaminated by strong surface waves (white ellipse) acquired in the field using sledge-hammer as a source. The source is located at 4 m lateral position. (b) The same shot gather after surface-wave suppression using a scheme involving seismic interferometry and adaptive subtraction. Note that events with negative moveout (yellow circle in Figure 3b) can now be identified.

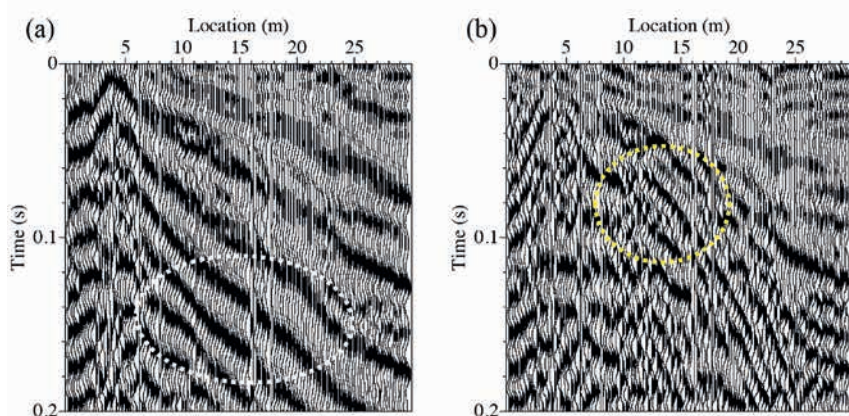


**Figure 4** As in Figure 3, but for seismic data acquired in the field using a shear-wave vibrator source.

a high-frequency horizontal (shear-wave) vibrator (Ghose et al., 1996; Ghose, 2002) as seismic sources. The reason we used shear waves is because of their relatively low propagation velocity in soft soils - resulting in short wavelength, hence high resolution. In addition, shear waves are directly related to the small-strain rigidity and are quite sensitive to subtle changes in the subsoil mechanical properties (e.g., Ghose and Goudswaard, 2004; Ghose, 2012; Ghose et al., 2013). The source-receiver geometry used to record the impulsive hammer data was the same as the one applied to generate the synthetic data discussed above. We covered 41 source positions at an interval of 1 m to acquire the shear-wave vibrator data. To compare the diffraction section from the vibrator data with the one from the sledge-hammer data, we select only vibrator shots whose positions coincided with those of the sledge-hammer source.

Figure 3a shows a typical raw common-source gather using the sledge-hammer as a source, while Figure 4a shows an example of shot gather using the vibrator at the same lateral location, after cross-correlation of the raw vibrograms with the source-monitor signal. The pre-processing steps for these two gathers are identical: trace editing, statics corrections, geometrical-spreading correction, and band-pass filtering. In addition, automatic gain control (AGC) with a window length of 30 ms is applied to both raw gathers for display purpose. Due to the soft soil condition in the near-surface, we notice that the raw data are dominated by the presence of strong surface waves (white ellipses in Figures 3a and 4a). These surface waves make the identification of weak diffraction events nearly impossible. To reveal the scattered energy, we apply the scheme that we have described above to attenuate the high-amplitude surface waves.



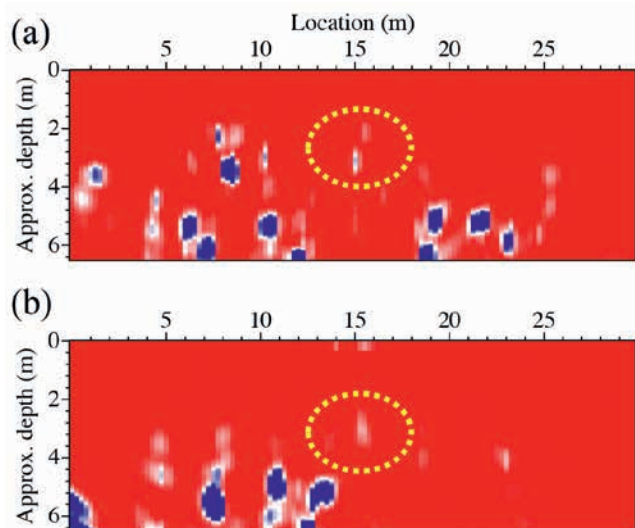


**Figure 5** Diffraction imaging result obtained from seismic data after surface-wave suppression: (a) sledge-hammer data; (b) shear-wave vibrator data.

The data after surface-wave suppression are shown in Figures 3b and 4b, respectively, where the yellow ellipses indicate some meaningful scattered events caused by small objects in the subsurface. We make such interpretations based on the negative moveouts of these events and consistently similar locations as revealed in two different datasets. Figure 5 illustrates the two final diffraction sections obtained from the hammer and vibrator data (after surface-wave suppression) using our new imaging approach. The velocity range we use for diffraction summation is from 120–140 m/s, with a step of 5 m/s. We obtain this velocity range using the asymptotic approach proposed by Shtivelman et al. (2009). In Figure 5, the vertical axis indicates the approximate depth in metres, which is converted using a subsurface velocity of 130 m/s. High-amplitude anomalies (blue or light blue colour in Figure 5) indicate the locations of potential buried objects of archaeological importance.

Earlier in a separate work, archaeologists collected samples from closely spaced shallow boreholes at this site. These samples indicate that the burial mound consists of sand and gravel at the shallow part down to around 3 m. Based on these samples, a cross-section of the subsurface of Mound B4749 was made, and is illustrated in Figure 6. The vertical axis in Figure 6 indicates depth in metres below the Amsterdam Ordnance Datum (*Normaal Amsterdams Peil* or NAP). In Figure 6, two distinguished features (primary mound and secondary mound) can be identified and

are interpreted as mounds constructed at different time periods. A magnetometry survey (Lambers et al., 2013) was also carried out at this site, where strong thermoremanent magnetization at the range of  $\pm 5 - 8$  nT was detected. This anomalous value was probably caused by high temperatures, and indicates the existence of burnt stones inside this mound. From the magnetic map of this area, the possible location of pits containing burnt stones was interpreted, which is illustrated by the yellow ellipse in Figure 6, at a height about 30 m NAP, while its lateral location is centered around 15 m. Due to the strong impedance contrast at this location compared to the surrounding medium, the seismic response from these stones can be recorded as diffraction events. In our diffraction sections, anomalies located at a lateral position around 15 m (yellow ellipse in Figures 5a and 5b) can be identified. These positions seem to agree with the locations of the burial pits indicated in Figure 6. For other deeper prominent anomalies in our diffraction sections, we cannot find direct indications in the core profile because of the limited depth of the shallow boreholes. These anomalies need to be verified through further checks.

## Discussion and conclusions

Diffraction imaging is inherently a 3D problem because diffracted waves caused by scattering objects propagate in all directions. When the seismic data is acquired along a line below which the target objects are distributed, the imaging of such targets is reliable. If this is not the case, the location of the scatterers will be estimated at wrong depths, and/or the quality of imaging will be heavily deteriorated, due to the lack of diffraction energy captured by the receivers. For the archaeological site that we investigated, the borehole profile already shows that the shallow subsurface up to 3 m depth is composed of finer sand and gravelly soils, which can be considered as a very heterogeneous media for the used seismic wavelengths. The wavefield containing information from local heterogeneities under our 2D seismic line could be acquired; the buried objects manifest as events with negative moveouts (e.g., yellow circles in Figures 3b and 4b). This makes it possible to map the distribution of heterogeneities at this archaeological site using our 2D diffraction-imaging method.

The seismic data acquired at this site are dominated by strong surface waves. To increase the reliability of the diffraction imaging, a technique that consists of seismic interferometry and adaptive subtraction is first applied to the data for the suppression of high-amplitude surface-wave noise in a data-driven way. Weak diffractions from the subsurface objects become identifiable after

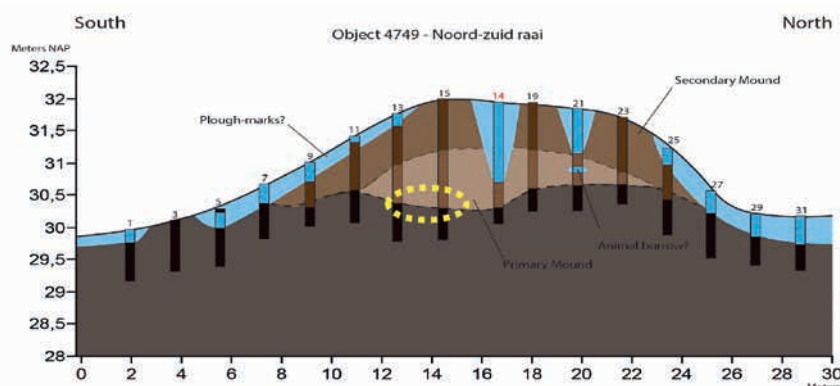


**Figure 6** Drawing of the same burial mound based on information of borehole samples. The lateral axis is the same as in Figure 5. The vertical axis indicates the height in metres using Amsterdam Ordnance Datum system (NAP). The location of a burial pit detected by magnetometry survey (Lambers et al., 2013) is marked by the yellow ellipse.

this procedure. These diffractions can be the input to our diffraction-imaging algorithm for locating the local, buried objects. Our diffraction-imaging method is based on optimal summation of seismic diffractions from these objects. An amplitude-unbiased coherency method is used to suppress the incoherent summation of noise, with the aim to enhance the weak and coherent diffracted signals. The stacking procedure results in a section where diffractions are emphasized and the remaining surface waves are further suppressed. This diffraction section can be useful for a reliable identification of the local heterogeneities. We demonstrate the reliability of the proposed diffraction imaging method using synthetic and field data.

## Acknowledgements

The first author would like to thank for financial support the China Scholarship Council (File No. 201604910851). We gratefully acknowledge the work done by Hendrik Pormes and Michael van de Stadt, which helped us to better interpret our results. We also appreciate all contributors of the open source community, whose tools and ideas inspired us to implement our method in a quick and efficient way.

## References

- Bracewell, R.N. [1986]. *The Fourier transform and its applications*. Vol. 31999, New York, McGraw-Hill.
- Bourgeois, Q. [2012]. *Monuments on the horizon: the formation of the barrow landscape throughout the 3<sup>rd</sup> and 2<sup>nd</sup> millennium BC*. Sidestone Press.
- Draganov, D., Wapenaar, K. and Thorbecke, J. [2006]. Seismic interferometry: reconstructing the Earth's reflection response. *Geophysics*, **71**(4), SI61-SI70.
- Fomel, S. [2008]. Adaptive multiple subtraction using regularized nonstationary regression. *Geophysics*, **74**(1), V25-V33.
- Ghose, R., Brouwer, J. and Nijhof, V. [1996]. A portable S-wave vibrator for high-resolution imaging of the shallow subsurface. *58<sup>th</sup> EAGE Conference and Exhibition*, Extended Abstracts.
- Ghose, R. [2002]. High-frequency shear wave reflections from shallow subsoil layers using a vibrator source: Sweep cross-correlation versus deconvolution with groundforce derivative. *SEG Annual Conference*, 408-1411.
- Ghose, R. and Goudswaard, J. [2004]. Integrating S-wave seismic-reflection data and cone penetration test data using a multiangle multiscale approach. *Geophysics*, **69**(2), 440-459.
- Ghose, R. [2012]. A microelectromechanical system digital 3C array seismic cone penetrometer. *Geophysics*, **77**(3), WA99-WA107.
- Ghose, R., Carvalho, J., and Loureiro, A. [2013]. Signature of fault zone deformation in near-surface soil visible in shear wave seismic reflections. *Geophysical Research Letters*, **40**(6), 1074-1078.
- Konstantaki, L.A., Draganov, D., Ghose, R. and Heimovaara, T. [2015]. Seismic interferometry as a tool for improved imaging of the heterogeneities in the body of a landfill. *Journal of Applied Geophysics*, **122**, 28-39.
- Lambers, L., Fassbinder, J.W.E., Lambers, K. and Bourgeois, Q.P.J. [2017]. The iron-age burial mounds of Epe-Nierson, the Netherlands: results from magnetometry in the range of  $\pm 1.0$  nT. *12<sup>th</sup> International Conference of Archaeological Prospection*, **12**, 132-134.
- Landa, E. and Keydar, S. [1998]. Seismic monitoring of diffraction images for detection of local heterogeneities. *Geophysics*, **63**(3), 1093-1100.
- Liu, J., Draganov, D. and Ghose, R. [2018]. Seismic interferometry facilitating the imaging of shallow shear-wave reflections hidden beneath surface waves. *Near Surface Geophysics*, **16**(3), 372-382.
- Schimmel, M. and Paulssen, H. [1997]. Noise reduction and detection of weak, coherent signals through phase-weighted stacks. *Geophysical Journal International*, **130**(2), 497-505.
- Shtivelman, V. and Keydar, S. [2005]. Imaging shallow subsurface inhomogeneities by 3D multipath diffraction summation. *First Break*, **23**(1), 39-42.
- Shtivelman, V., Keydar, S. and Mikenberg, M. [2009]. Imaging near-surface inhomogeneities using weighted multipath summation. *Near Surface Geophysics*, **7**(3), 171-177.
- Thorbecke, J.W. and Draganov, D. [2011]. Finite-difference modeling experiments for seismic interferometry. *Geophysics*, **76**(6), H1-H18.
- Wapenaar, K. and Fokkema, J. [2006]. Green's function representations for seismic interferometry. *Geophysics*, **71**(4), SI33-SI46.
- Walters, S.L., Miller, R.D., Steeples, D.W., Xia, J. and Zeng, C. [2009]. Detecting tunnels and underground facilities using diffracted P-waves. *SEG Annual Conference*, 937-942.

ADVERTISEMENT

**XtremeGeo**

Where Technology Comes to Earth

**FLATIRONS™**

Industry Leading  
First Break Picker  
Intuitive Geometry QC

Near - Surface Seismic  
Modeling and Imaging

Innovative Variable Node Spacing Tomography  
Stack-based Delay Time Analysis

Boulder, CO, USA +1720 255 2354 [xtgeo.com](http://xtgeo.com)